Seismic Moment Tensors in Anisotropic Media: A Review

Václav Vavryčuk

1 Introduction

Seismic anisotropy is a common property of rocks and geological structures in the Earth crust and in the upper mantle (Babuška and Cara 1991; Rabbel and Mooney 1996; Silver 1996; Savage 1999). It may be caused by sediment layering, by stress-aligned systems of microcracks, cracks or fractures, or by the textural ordering of rock-forming minerals. Anisotropy affects propagation of seismic waves as well as radiation of waves by seismic sources. So far seismologists have focused mainly on studying wave propagation in anisotropic media (e.g., Musgrave 1970; Helbig 1994; Červený 2001; Vavryčuk 2001b, 2003), and on observing the effects of anisotropy on seismic waves (Babuška and Cara 1991) as the directional variation of seismic velocities or shear-wave splitting, detected and measured in situ (Kaneshima et al. 1988; Crampin 1993; Savage 1999) or in the laboratory on rock samples (Kern and Schmidt 1990; Pros et al. 1998; Mainprice et al. 2000; Svitek et al. 2014).

However, equally important is the way in which anisotropy affects the radiation of waves from seismic sources. This comprises calculating the Green's functions (Burridge 1967; Ben-Menahem and Sena 1990a, b; Gajewski 1993; Vavryčuk 1997; Pšenčík 1998; Červený 2001; Vavryčuk 2007), seismic moment tensors and focal mechanisms in anisotropic media (Šílený and Vavryčuk 2000, 2002; Vavryčuk 2005). For example, Kawasaki and Tanimoto (1981) and Vavryčuk (2005) pointed out that shear faulting in anisotropic media can produce mechanisms with non-double couple (non-DC) components. Since the non-DC mechanisms of earthquakes are frequently observed (Miller et al. 1998), the problem, whether anisotropy contributes to them or not, is not only of theoretical interest but also of practical relevance. Anisotropy as a possible origin of non-DC mechanisms has been mentioned and discussed also by other authors (Kawakatsu 1991; Frohlich 1994; Julian et al. 1998; Vavryčuk 2002, 2004, 2006; Rössler et al. 2003; Vavryčuk et al. 2008).

V. Vavryčuk (✉)
Institute of Geophysics, Czech Academy of Sciences, Boční II/1401, 141 31
Praha 4, Czech Republic
e-mail: vv@ig.cas.cz

29

Since the effects of anisotropy on focal mechanisms and moment tensors are still not well known and often neglected, I present a review of basic properties of moment tensors in anisotropic media. The review covers theory, numerical modelling and several applications to earthquakes on various scales including acoustic emissions measured in the lab, microearthquakes in the upper crust and large deep-focus earthquakes in a subducting slab. The goal is to point out errors introduced when seismic anisotropy is neglected in moment tensor inversions, and a possibility to study seismic anisotropy using accurately determined moment tensors.

2 Theory

2.1 *Moment Tensor in Anisotropic Media*

Moment tensor $\mathbf{M}$ of a seismic source in an anisotropic medium is expressed as (Aki and Richards 2002, Eq. 3.19)

$$M_{ij} = uSc_{ijkl}v_k n_l, \tag{1}$$

where u is the slip, S is the fault area, c_{ijkl} are the elastic stiffness parameters of the medium surrounding the fault, $\mathbf{v}$ is the slip direction, and $\mathbf{n}$ is the fault normal. Introducing source tensor $\mathbf{D}$ as

$$D_{kl} = \frac{uS}{2}\left(v_k n_l + v_l n_k\right), \tag{2}$$

and taking into account the symmetry of c_{ijkl}, we can express Eq. (1) in the following form

$$M_{ij} = c_{ijkl}D_{kl}, \tag{3}$$

which resembles the Hooke's law

$$\tau_{ij} = c_{ijkl}e_{kl}, \tag{4}$$

expressing the relation between stress and strain tensors τ_{ij} and e_{ij} in elastic media. Therefore, Eq. (3) can be called as "the generalized Hooke's law at the source". Source tensor $\mathbf{D}$ defines geometry of dislocation at the source being an analogue to strain tensor e_{ij}. Moment tensor $\mathbf{M}$ defines the equivalent body forces acting at the source being an analogue to stress tensor τ_{ij}.

Equation (3) can equivalently be expressed in matrix form as

$$\mathbf{m} = \mathbf{Cd}, \tag{5}$$

where $\mathbf{C}$ is the 6×6 matrix of the elastic parameters in the two-index Voigt notation, where the pairs of the subscripts in the four-index tensor c_{ijkl} are substituted in the following way: $11 \rightarrow 1, 22 \rightarrow 2, 33 \rightarrow 3, 23 \rightarrow 4, 13 \rightarrow 5$ and $12 \rightarrow 6$ (see Musgrave 1970, Eq. 3.13.4). Quantities $\mathbf{m}$ and $\mathbf{d}$ are the 6-vectors defined as

$$\mathbf{m} = (M_{11}, M_{22}, M_{33}, M_{23}, M_{13}, M_{12})^{T}, \tag{6}$$

$$\mathbf{d} = uS\,(n_1 v_1, n_2 v_2, n_3 v_3, n_2 v_3 + n_3 v_2, n_1 v_3 + n_3 v_1, n_1 v_2 + n_2 v_1)^{T}. \tag{7}$$

Source tensor $\mathbf{D}$ is expressed by the components of vector $\mathbf{d}$ as follows:

$$\mathbf{D} = \frac{1}{2} \begin{bmatrix} 2d_1 & d_6 & d_5 \\ d_6 & 2d_2 & d_4 \\ d_5 & d_4 & 2d_3 \end{bmatrix}. \tag{8}$$

The moment tensor $\mathbf{M}$ of a seismic source in an isotropic medium reads (Aki and Richards 2002, Eq. 3.21)

$$M_{ij} = \lambda D_{kk} \delta_{ij} + 2\mu D_{ij}, \tag{9}$$

with the trace

$$M_{kk} = (3\lambda + 2\mu)\,D_{kk}, \tag{10}$$

where λ and μ are the Lamé constants describing the isotropic medium surrounding the fault, and δ_{ij} is the Kronecker delta.

2.2 Eigenvalues and Eigenvectors of Tensors M and D

Tensor $\mathbf{M}$ has a diagonal form expressed by three eigenvalues M_1, M_2 and M_3

$$\mathbf{M}^{diag} = \begin{bmatrix} M_1 & 0 & 0 \\ 0 & M_2 & 0 \\ 0 & 0 & M_3 \end{bmatrix}, \text{ where } M_1 \geq M_2 \geq M_3. \tag{11}$$

In isotropic media, Eq. (11) reads

$$\mathbf{M}^{diag} = uS \begin{bmatrix} (\lambda + \mu)\,\mathbf{n} \cdot \mathbf{v} + \mu & 0 & 0 \\ 0 & \lambda \mathbf{n} \cdot \mathbf{v} & 0 \\ & & (\lambda + \mu)\,\mathbf{n} \cdot \mathbf{v} - \mu \end{bmatrix}. \tag{12}$$

where $\mathbf{n} \cdot \mathbf{v}$ is the scalar product of two unit vectors $\mathbf{n}$ and $\mathbf{v}$,

Fig. 1 Model of a
shear-tensile earthquake.
Vector **u** is the slip vector,
vector **n** is the fault normal,
and α is the slope angle.
Angle β is defined as
$\beta = (90° - \alpha)/2$
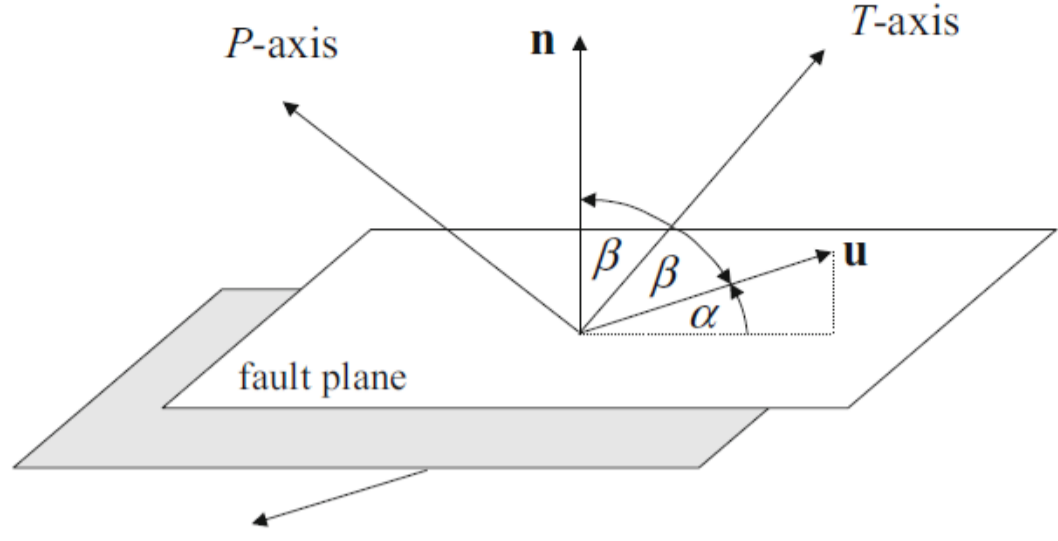
$$\mathbf{n} \cdot \mathbf{v} = n_1 v_1 + n_2 v_2 + n_3 v_3. \tag{13}$$

A diagonal form of tensor **D** is independent of elastic properties of the medium being expressed as

$$\mathbf{D}^{diag} = \begin{bmatrix} D_1 & 0 & 0 \\ 0 & D_2 & 0 \\ 0 & 0 & D_3 \end{bmatrix} = \frac{uS}{2} \begin{bmatrix} \mathbf{n} \cdot \mathbf{v} + 1 & 0 & 0 \\ 0 & 0 & 0 \\ 0 & 0 & \mathbf{n} \cdot \mathbf{v} - 1 \end{bmatrix}. \tag{14}$$

The determinant of **D** is zero and the trace of **D** is

$$D_{kk} = uS (\mathbf{n} \cdot \mathbf{v}) = uS \sin \alpha, \tag{15}$$

where α is the slope angle defined as the deviation of the slip vector **n** from the fault plane (Vavryčuk 2001a, b, 2011).

The eigenvectors of tensors **M** and **D** specify the coordinate systems in which these tensors are diagonalized. The eigenvectors of **M** are denoted as the P, T and B axes and correspond to minimum eigenvalue M_3, maximum eigenvalue M_1, and intermediate eigenvalue M_2, respectively. Physically, the P, T and B axes are directions of the maximum compressional, maximum tensional and intermediate stresses generated at the source.

The eigenvectors of moment tensor **M** are generally different from those of source tensor **D**. However, the both coordinate systems coincide in isotropic media. In this case, the B axis is perpendicular to fault normal **n** and slip direction **v**. The P and T axes lie in the plane defined by vectors **n** and **v** (Fig. 1) being expressed as

$$\mathbf{t} = \frac{\mathbf{n} + \mathbf{v}}{|\mathbf{n} + \mathbf{v}|}, \mathbf{b} = \mathbf{n} \otimes \mathbf{v}, \mathbf{p} = \frac{\mathbf{n} - \mathbf{v}}{|\mathbf{n} - \mathbf{v}|}, \tag{16}$$

where **p**, **t**, and **b** are the directional vectors of the P, T and B axes, respectively, and symbol $\otimes$ denotes the vector product.

Fig. 2 Model of shear (**a**), tensile (**b**) and compressive (**c**) faulting. Vector **u** is the slip vector, α is the slope angle

(a) Shear faulting

(b) Tensile faulting

(c) Compressive faulting
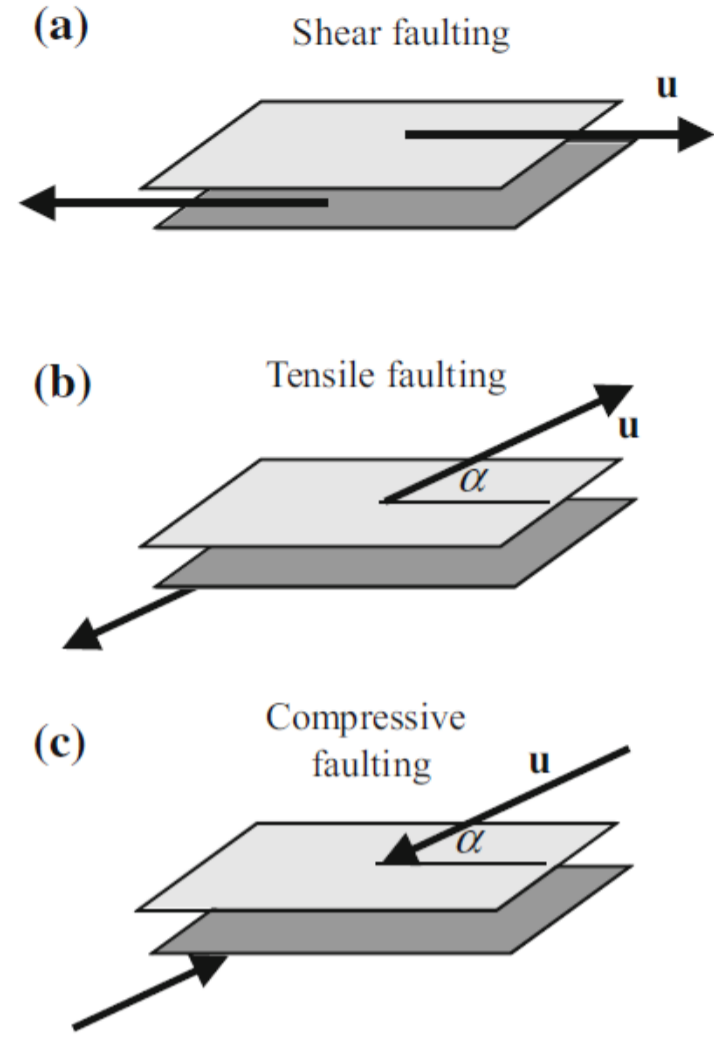
2.3   Tensile Faulting in Isotropic Media Versus Shear Faulting in Anisotropic Media

For shear faulting, slope angle α is zero (Fig. 2a) and Eqs. (12) and (14) for **M** and **D** further simplify in isotropic media to

$$\mathbf{M}^{diag} = \mu u S \begin{bmatrix} +1 & 0 & 0 \\ 0 & 0 & 0 \\ 0 & 0 & -1 \end{bmatrix}, \mathbf{D}^{diag} = \frac{uS}{2} \begin{bmatrix} +1 & 0 & 0 \\ 0 & 0 & 0 \\ 0 & 0 & -1 \end{bmatrix} \tag{17}$$

being known as the double-couple (DC) tensors.

For tensile/compressive faulting (Fig. 2b, c), slope α is non-zero and tensors **M** and **D** of a source in isotropic media contain also non-double-couple (non-DC) components. The non-DC components are usually decomposed into the isotropic (ISO) and compensated linear vector dipole (CLVD) parts (see Vavryčuk 2015). For tensor **D**, the relative amounts of ISO and CLVD depend on the slope angle; for tensor **M**, the ISO and CLVD depend on the slope and on the ratio of the *P*- and *S*-wave velocities *vp/vs*.

For moment tensors in anisotropic media, the problem is more involved. In anisotropic media, even shear faulting on a planar fault produces a generally non-DC moment tensor. This is caused by the elasticity tensor in Eq. (3) which is formed by 21 elastic parameters. However, the moment tensor is simplified for anisotropy of higher symmetry. For example, under orthorhombic symmetry, **M** is also a pure DC provided that fault normal **n** coincides with the symmetry axis and slip **u** lies in the
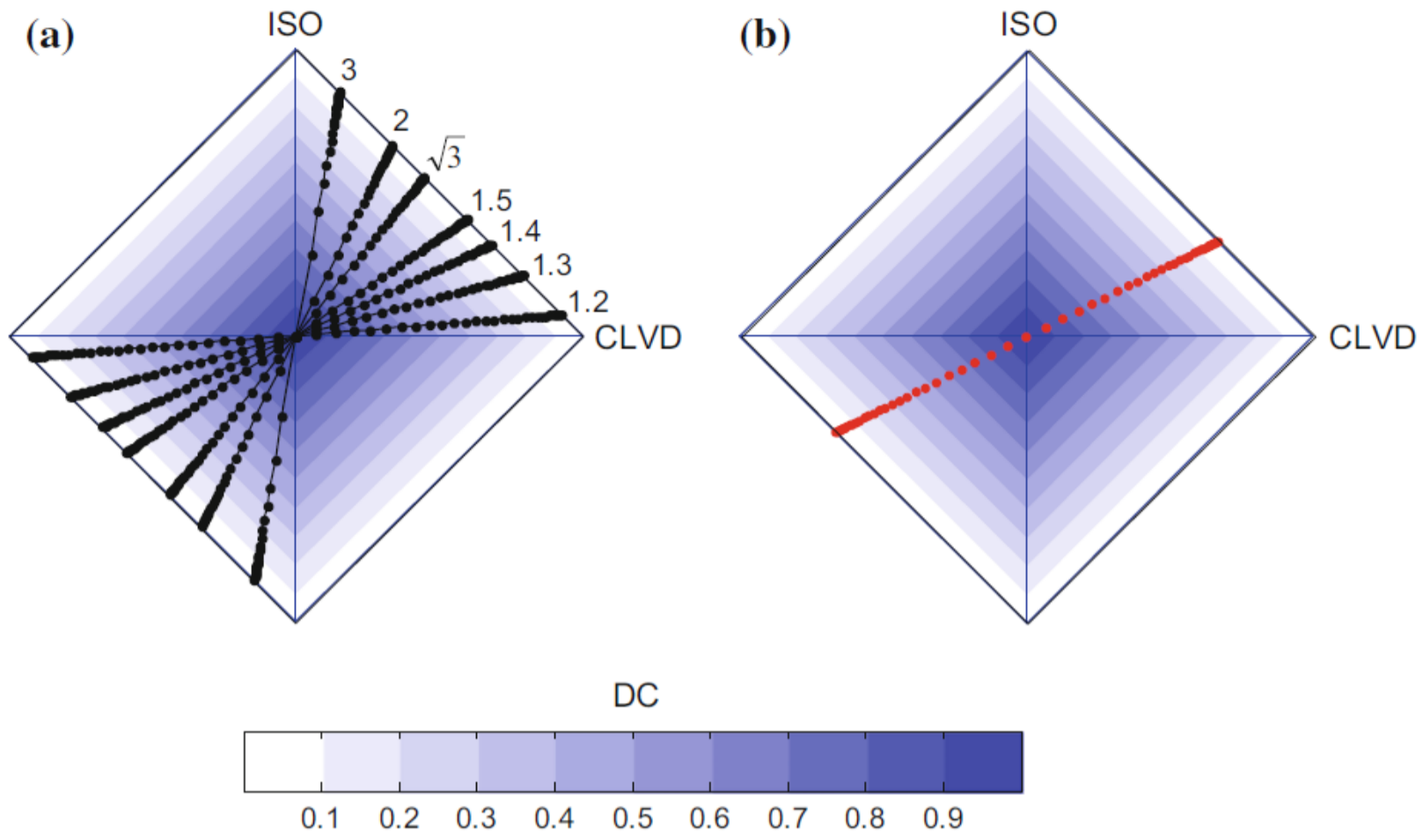
Fig. 3 The source-type plots for the moment tensors (**a**) and source tensors (**b**) for shear-tensile-compressive faulting in isotropic media. Red dots—the source tensors, black dots—the moment tensors. Isotropic media in (**a**) are characterized by various values of the v_P/v_S ratios (the values are indicated in the plot). The dots in (**a**) and (**b**) correspond to the sources with a specific value of the slope angle (i.e. the deviation of the slip vector from the fault). The slope angle ranges from $-90°$ (pure compressive crack) to $90°$ (pure tensile crack) in steps of $3°$. For a detailed explanation of properties of the source-type plot, see Vavryčuk (2015). After Vavryčuk (2015)

symmetry plane (but not along the symmetry axis). However, the orientation of the DC can deviate from the plane defined by the fault normal and slip direction (see Vavryčuk 2005).

The properties of the moment and source tensor decompositions for shear and tensile sources in isotropic and anisotropic media are illustrated in Figs. 3 and 4. Figure 3 shows the source-type plots for shear-tensile-compressive sources with a variable slope angle α (i.e. the deviation of the slip vector from the fault, see Vavryčuk 2011) situated in an isotropic medium. The plot shows that the scale factors of the ISO and CLVD components are linearly dependent for both moment and source tensors. For the moment tensors, the line direction depends on the v_P/v_S ratio (Fig. 3a); for the source tensors, the line is independent of the properties of the elastic medium and the ISO/CLVD ratio is always 1/2 (Fig. 3b). This property of the source tensors is preserved even for anisotropic media.

On the contrary, the moment tensors can behave in a more complicated way in anisotropic media. Figure 4 shows the ISO and CLVD components of the moment tensors of shear (Fig. 4a) or shear-tensile (Fig. 4b) faulting in the Bazhenov shale (Vernik and Liu 1997). This complicated behaviour prevents a straightforward interpretation of moment tensors in terms of physical faulting parameters. Therefore, first the source tensors must be calculated from moment tensors and then interpreted.
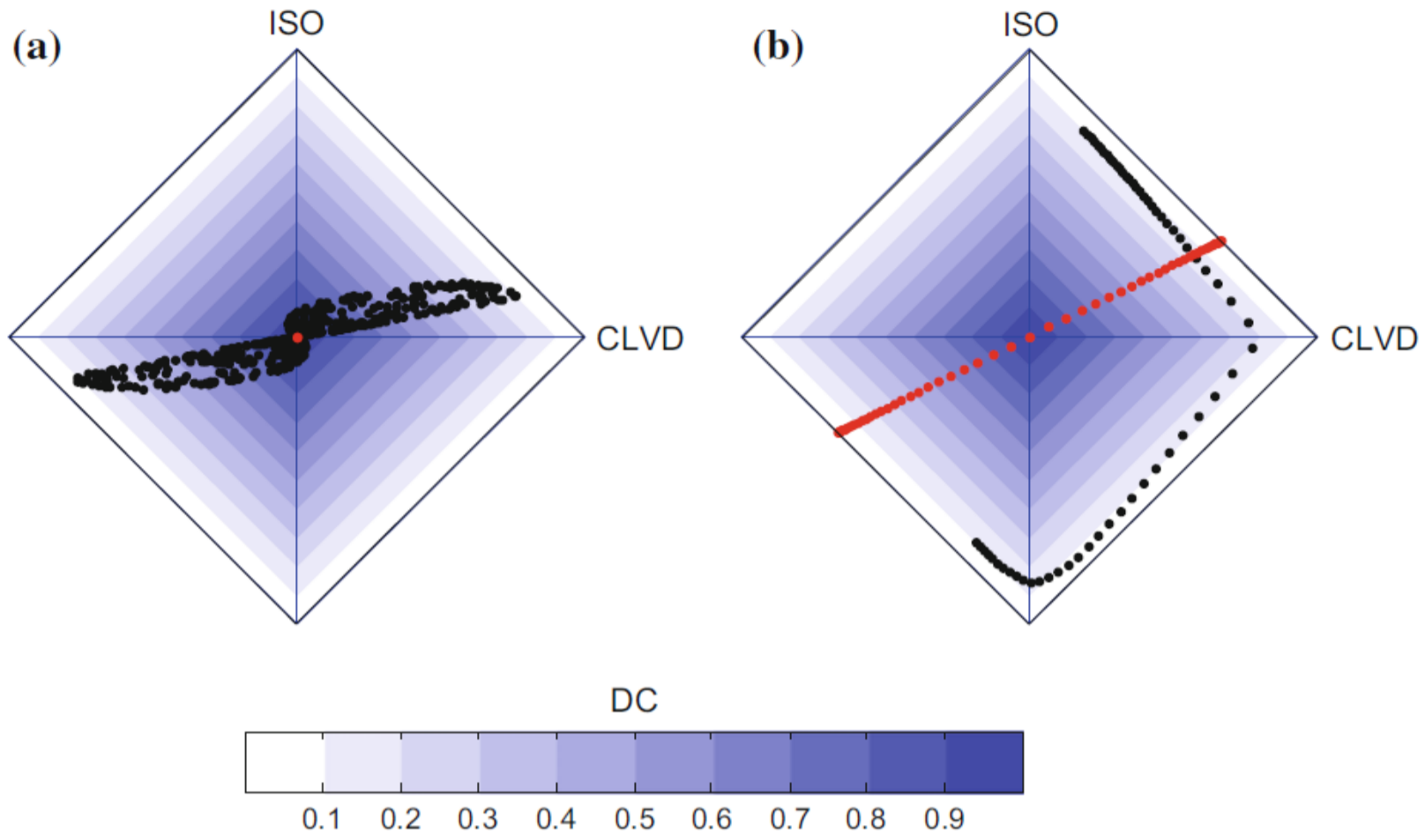
Fig. 4 The source-type plots for the moment and source tensors for shear (**a**) and shear-tensile-compressive (**b**) faulting in anisotropic media. Red dots—the source tensors, black dots—the moment tensors. The black dots in (**a**) correspond to 500 moment tensors of shear sources with randomly oriented faults and slips. The black dots in (**b**) correspond to the moment tensors of shear-tensile sources with strike = $0°$, dip = $20°$ and rake = $-90°$ (normal faulting). The slope angle ranges from $-90°$ (pure compressive crack) to $90°$ (pure tensile crack) in steps of $3°$. The medium in (**a**) and (**b**) is transversely isotropic with the following elastic parameters (in 10^9 kg m^{-1}s^{-2}): $c_{11} = 58.81$, $c_{33} = 27.23$, $c_{44} = 13.23$, $c_{66} = 23.54$ and $c_{13} = 23.64$. The medium density is 2500 kg/m^3. The parameters are taken from Vernik and Liu (1997) and describe the Bazhenov shale (depth of 12,507 ft.). After Vavryčuk (2015)

2.4   Inversion for Geometry of Faulting

In order to determine fault normal **n** and slip direction **v** from moment tensor **M** and from matrix of elastic parameters **C**, we have to calculate vector **d** from Eq. (5),

$$\mathbf{d} = \mathbf{C}^{-1}\mathbf{m}, \tag{18}$$

and subsequently we construct source tensor **D** using Eq. (8). Diagonalizing **D**, we obtain eigenvalues D_1 and D_3, and eigenvectors $\mathbf{e}_1$, $\mathbf{e}_2$, and $\mathbf{e}_3$. The slope angle α between the fault plane and slip direction is determined from the trace of **D**, see Eq. (15)

$$\sin\alpha = \frac{1}{uS}\mathrm{Tr}\,(\mathbf{D}) = \frac{D_1 + D_3}{D_1 - D_3}. \tag{19}$$

Vectors **n** and **v** are determined from the eigenvectors and eigenvalues of **D**

$$\mathbf{n} = \frac{1}{\sqrt{D_1 - D_3}} \left(\sqrt{|D_1|} \mathbf{e}_1 + \sqrt{|D_3|} \mathbf{e}_3 \right), \tag{20}$$

$$\mathbf{v} = \frac{1}{\sqrt{D_1 - D_3}} \left(\sqrt{|D_1|} \mathbf{e}_1 - \sqrt{|D_3|} \mathbf{e}_3 \right). \tag{21}$$

For shear sources $(\mathbf{n} \perp \mathbf{v})$,

$$\mathrm{Tr}\,(\mathbf{D}) = 0, \; D_1 = \frac{uS}{2} \text{ and } D_3 = -\frac{uS}{2}, \tag{22}$$

hence

$$\mathbf{n} = \frac{1}{\sqrt{2}} \left(\mathbf{e}_1 + \mathbf{e}_3 \right), \, \mathbf{v} = \frac{1}{\sqrt{2}} \left(\mathbf{e}_1 - \mathbf{e}_3 \right). \tag{23}$$

It follows from the symmetry of fault normal $\mathbf{n}$ and slip direction $\mathbf{v}$ in Eq. (2) that the solution for $\mathbf{n}$ and $\mathbf{v}$ is ambiguous and the plus and minus signs in (20–21) and (23) can be interchanged.

2.5 *Inversion for Anisotropy*

If elastic parameters of the medium are not known, we can invert moment tensors $\mathbf{M}$ jointly for the source tensors $\mathbf{D}$ of individual earthquakes and for elastic parameters $\mathbf{C}$ in the focal zone using the following equation

$$\mathbf{Cd} = \mathbf{m}. \tag{24}$$

The right-hand side of Eq. (24) represents observations (i.e. a set of moment tensors), and the left-hand side of Eq. (24) is unknown being a product of unknown elastic parameters $\mathbf{C}$ and unknown geometry of faulting $\mathbf{d}$ for a set of earthquakes. The elastic parameters $\mathbf{C}$ are common for all earthquakes, while vector $\mathbf{d}$ is specific for each earthquake.

Since source tensor $\mathbf{D}$ is formed by a dyad of vectors $\mathbf{v}$ and $\mathbf{n}$, it should always have one zero eigenvalue, and subsequently its determinant must be zero:

$$\mathrm{Det}\,(\mathbf{D}) = 0. \tag{25}$$

If faulting is shear, tensor $\mathbf{D}$ is constrained to have also zero trace

$$\mathrm{Trace}\,(\mathbf{D}) = uS\,(\mathbf{n} \cdot \mathbf{v}) = 0. \tag{26}$$

Equations (25–26) can be used for defining the misfit function in the inversion for anisotropy. If we know moment tensors of many earthquakes that occurred at the

Table 1 Elastic parameters of the dry and water-filled crack models

Model	C_{11}	C_{22}	C_{33}	C_{44}	C_{55}	C_{66}	C_{12}	C_{13}	C_{23}
Dry cracks	53.51	53.51	33.35	14.28	14.28	17.86	17.79	12.32	12.32
Water-filled cracks	56.62	56.62	56.11	14.28	14.28	17.86	20.90	20.75	20.75

Elastic parameters C_{ij} are in 10^9 kg m^{-1} s^{-2}

same source area, we can invert for elastic parameters c_{ijkl} minimizing the sum of absolute values of Det(**D**) for all earthquakes. This can be applied to shear as well as non-shear earthquakes. If we are confident that the studied earthquakes are shear, we can minimize the sum of absolute values of Det(**D**) and Trace(**D**) for all earthquakes. The method can be modified to be applicable also to the inversion of moment tensors constrained to have the zero trace (see Vavryčuk 2004).

The extent and quality of a set of moment tensors limits the number of anisotropic parameters, which can be inverted for. A general triclinic anisotropy is described by 21 elastic parameters c_{ijkl}. However, two of them must always be fixed to overcome the problem of coupling between elastic parameters c_{ijkl}, slip u and fault area S in Eq. (26) under shear faulting. Hence, for isotropy, which is described by two parameters, no information on the medium can be gained from moment tensors of shear earthquakes, but the *vp/vs* ratio can be determined from moment tensors of tensile/compressive earthquakes (Fig. 3a).

3   Numerical Modelling

A sensitivity of moment tensors to seismic anisotropy is exemplified on two models displaying effective transverse isotropy (TI) produced by presence of preferentially aligned cracks. Figure 5 shows phase velocities for the dry and water-filled crack models (see Hudson 1981; Shearer and Chapman 1989) and Table 1 summarizes their elastic parameters. Anisotropy strength of the *P*, *SV* and *SH* waves is 23.5, 1.3, and 11.2% for dry cracks, and 3.5, 11.0 and 11.2% for the water-filled cracks.

3.1   Non-DC Components Produced by Shear Faulting

As mentioned above, shear faulting in anisotropic media can generate non-DC components in moment tensors. The non-DC components depend on type and strength of anisotropy and on the orientation of faulting. Figure 6 shows the ISO and CLVD percentages for a fixed geometry of faulting: the fault normal is along the *z*-axis and the slip along the *x*-axis. Such faulting generates no ISO and CLVD for TI with
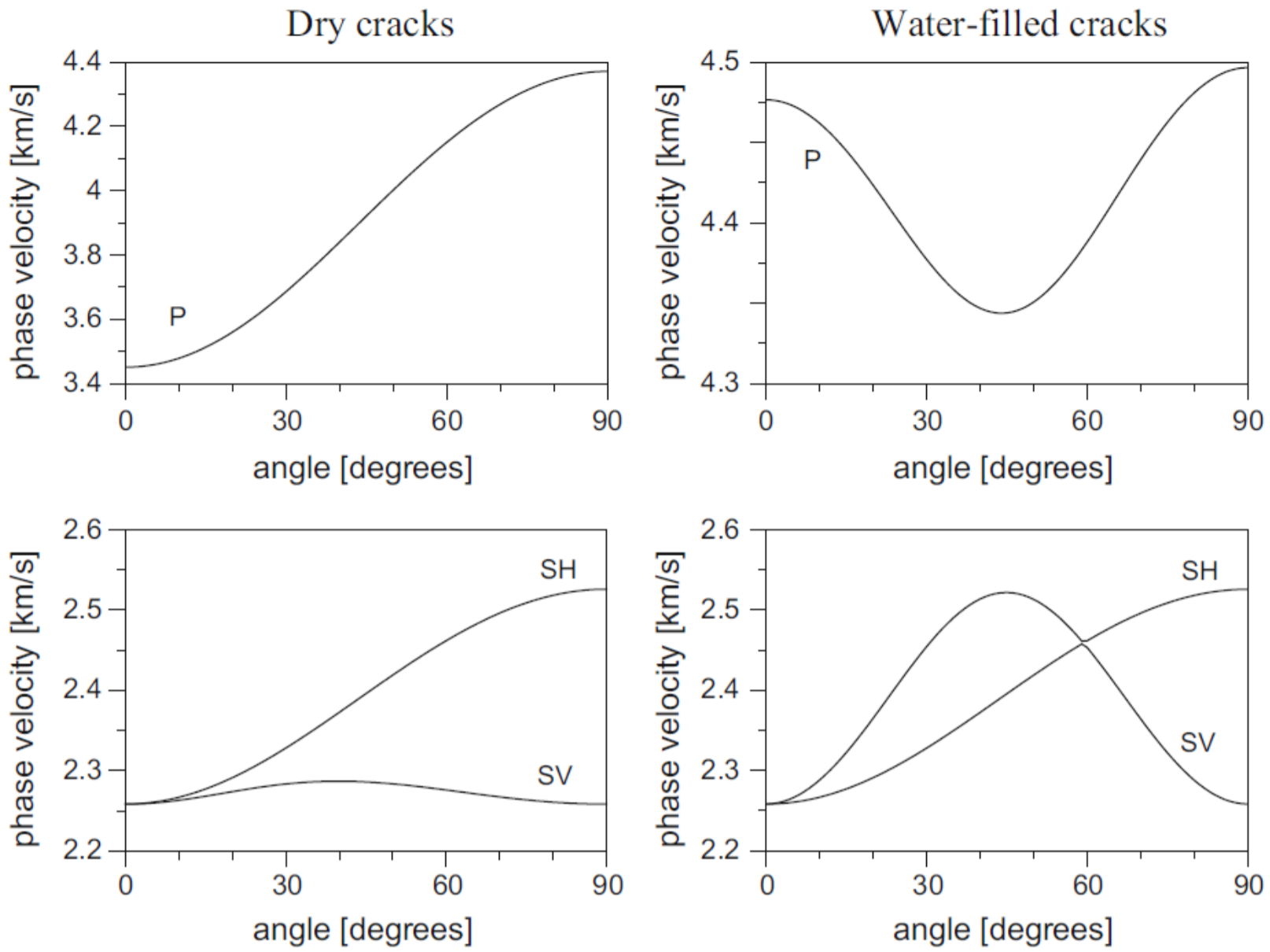
Fig. 5 Phase velocities of *P* (upper plots) and *S* (lower plots) waves as a function of the deviation of the wave normal from the symmetry axis for the model of dry cracks (left-hand plots) and water-filled cracks (right-hand plots)

a vertical symmetry axis. However, if the symmetry axis is inclined, the ISO and CLVD become non-zero. The values of the ISO and CLVD are shown as a function of direction of the symmetry axis for the dry crack model (Fig. 6, left-hand plots) and the water-filled crack model (Fig. 6, right-hand plots).

For the model of dry cracks, the percentages of the ISO and CLVD are in the intervals: (–20.7, 20.7) and (–16.1, 16.1), respectively (see Table 2). For the model of water-filled cracks, the percentages of the ISO and CLVD are in the intervals: (–0.6, 0.6) and (–19.9, 19.9), respectively. Hence, the shear source produces remarkable non-DC components in both anisotropy models. For dry cracks, both ISO and CLVD are high. On the contrary, water-filled cracks produce a high CLVD, but almost zero ISO. Despite the different percentages of the ISO in both models, their directional variation is similar. Interestingly, the directional variations of the CLVD are quite different for both models, the variation for water-filled cracks being more complicated than for dry cracks.
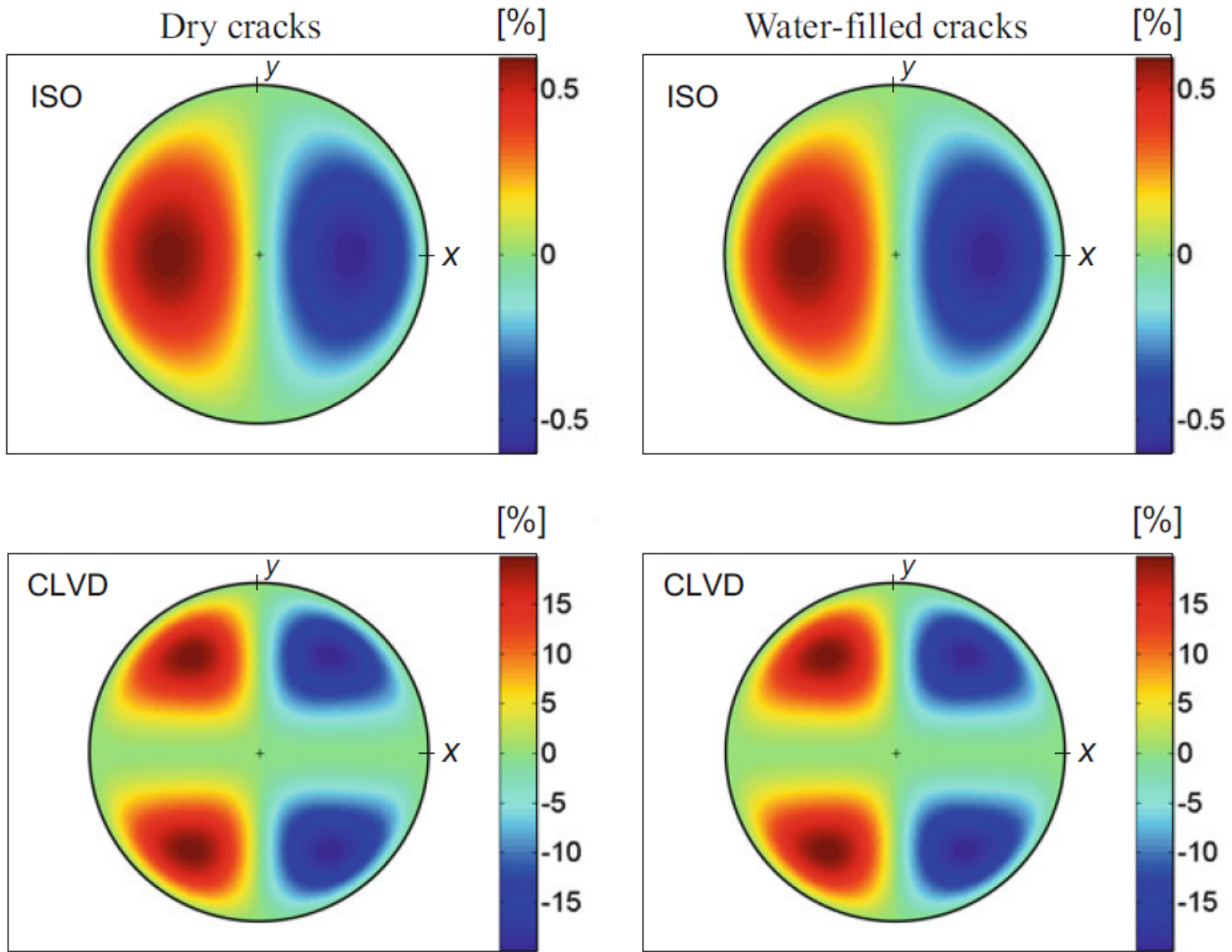
Fig. 6 The percentages of the non-DC components generated by shear faulting in the dry crack model (left-hand plots) and water-filled crack model (right-hand plots) with an inclined symmetry axis. Geometry of faulting is fixed: $\mathbf{n} = (0, 0, 1)^T$, $\mathbf{v} = (1, 0, 0)^T$. Points inside the circle correspond to TI with a varied orientation of the symmetry axis. The plus sign marks the TI with the vertical symmetry axis, the points along the circle correspond to the TI with the horizontal symmetry axes. The colour indicates the value of the non-DC component. Equal-area projection is used. The CLVD and ISO percentages are calculated by using Eq. (8) of Vavryčuk (2001a)

3.2   Spurious Rotation of a Fault Normal and Slip Direction

Fault plane solutions are usually calculated under the assumption of an isotropic focal area. If the focal area is anisotropic, the procedure yields distorted results. The errors owing to neglecting of anisotropy are illustrated for the dry crack model (Fig. 7, left-hand plots) and for the water-filled crack model (Fig. 7, right-hand plots). The upper/lower plots in the figures show the deviation between the true and approximate fault normals/slip directions. The approximate values were calculated from the eigenvectors of the moment tensor using the following standard formulae:

$$\mathbf{n}^{approx} = \frac{1}{\sqrt{2}} \left(\mathbf{p} + \mathbf{t} \right), \tag{27}$$

$$\mathbf{v}^{approx} = \frac{1}{\sqrt{2}} \left(\mathbf{p} - \mathbf{t} \right), \tag{28}$$

Table 2 Average velocities, anisotropy strength and non-DC components produced by shear faulting in the crack models

Model	v_P [km/s]	v_S [km/s]	a_P [%]	a_{SV} [%]	a_{SH} [%]	$CLVD^{MAX}$ [%]	ISO^{MAX} [%]	DC^{MIN} [%]	δ^{MAX} [°]
Dry cracks	3.92	2.33	23.5	1.3	11.2	16.1	20.7	64.3	6.4
Water filled cracks	4.42	2.39	3.5	11.0	11.2	19.9	0.6	79.8	6.4

a_P, a_{SV}, a_{SH} denote the anisotropy strength for the P, SV and SH waves The percentage of anisotropy strength is defined as $a = 200 \left(v^{MAX} - v^{MIN}\right)/\left(v^{MAX} + v^{MIN}\right)$, where v^{MAX} and v^{MIN} are the maximum and minimum phase velocities of the respective wave. $CLVD^{MAX}$, ISO^{MAX}, DC^{MIN} and δ^{MAX} are the maximum absolute values of the CLVD and ISO, the minimum value of the DC and the maximum deviation of the approximate fault normal and slip direction from true values observed in the specified anisotropy, respectively. The DC, CLVD and ISO percentages are calculated by using Eqs. (8a–c) of Vavryčuk (2001a)

where **p** and **t** are the unit eigenvectors of the moment tensor corresponding to the P and T axes. Because of the ambiguity of the solution for the fault normal and slip, we selected the pair of $\mathbf{n}^{approx}$ and $\mathbf{v}^{approx}$ which approximated the true vectors better.

Figure 7 shows that the maximum deviation between the true and approximate fault normals and slips attains coincidently a value of 6.4° for both crack models. This indicates that the deviation is not sensitive to strength of the P-wave anisotropy, which is different in the models, but rather to strength of the S-wave anisotropy. The maximum deviation of 6.4°, corresponding to the S-wave anisotropy of 11.2%, is not very high, but it can still introduce a non-negligible bias in carefully determined focal mechanisms. Similarly as for the CLVD, the directional variation of the deviations is more complicated for water-filled cracks than for dry cracks.

4   Applications

Let us illustrate the sensitivity of moment tensors to seismic anisotropy on three real datasets covering a broad range of scales: (1) acoustic emissions generated in the lab, (2) microearthquakes produced by fluid injection in the Earth's crust, and (3) large deep-focus earthquakes in the Tonga subduction zone.

4.1   *Acoustic Emissions in Anisotropic Rocks*

Laboratory experiments are advantageous for the analysis of sensitivity of moment tensors to seismic anisotropy because: (1) they are carried out under controlled conditions; (2) the physical parameters of the rock sample can be accurately monitored;
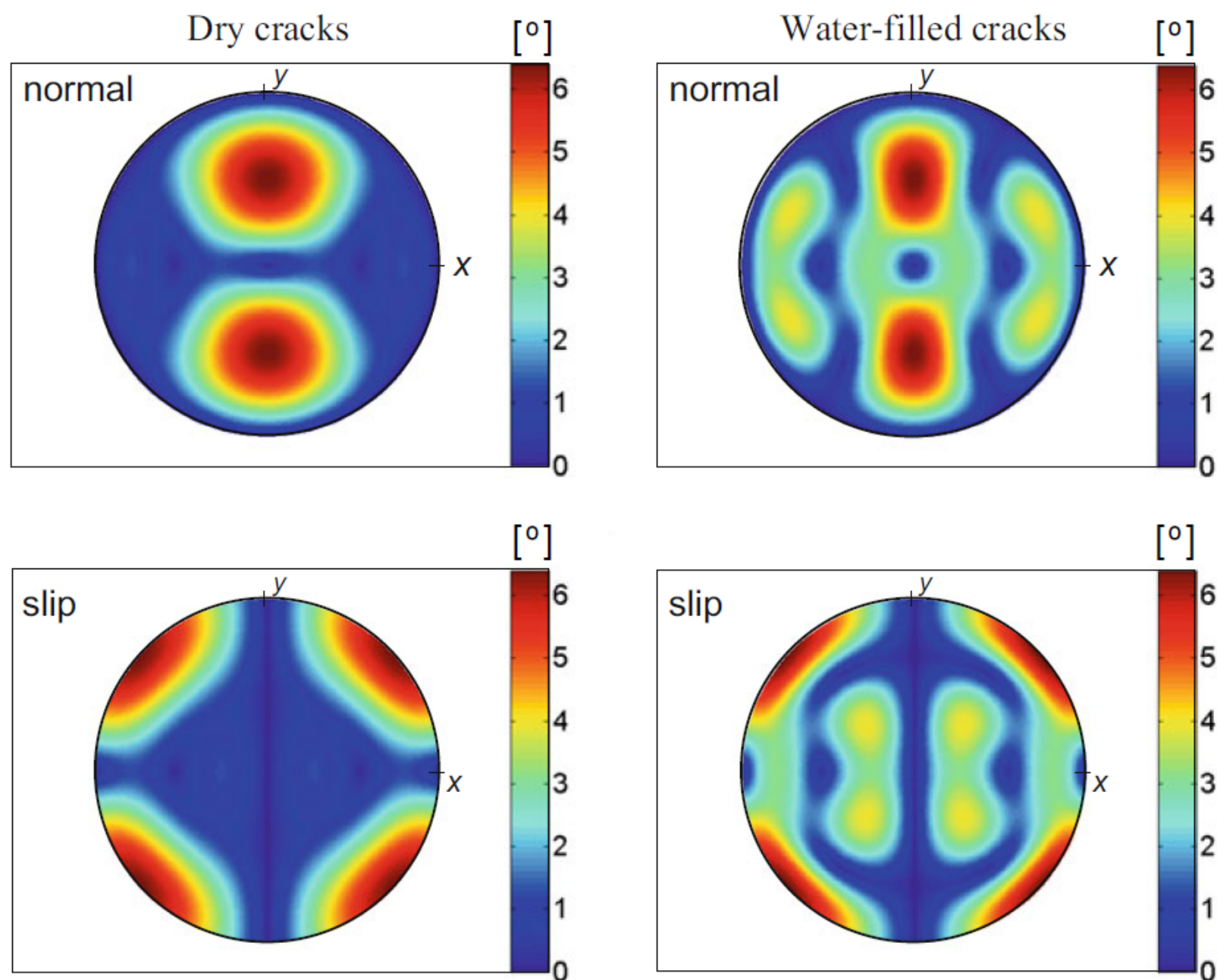
Fig. 7 The deviation between the true and approximate fault normals (upper plots), and between the true and approximate slip directions (lower plots) for the dry crack model (left-hand plots) and water-filled crack model (right-hand plots) with an inclined symmetry axis. The centre of the circle corresponds to the TI with the vertical symmetry axis, the points along the circle correspond to the TI with the horizontal symmetry axes. The colour indicates the angular deviation. Equal-area projection is used. The deviation is in degrees

(3) the rock samples can display various levels of anisotropy, and (4) the loading of the rocks samples produces large sets of acoustic emissions (AEs) suitable for a robust statistical analysis.

Stierle et al. (2016) analysed acoustic emission data measured by Stanchits et al. (2006) during triaxial compression experiments on a granite sample. The cylindrical sample (diameter 50 mm, length 100 mm) was subjected to a differential stress cycle at horizontal confining pressure of 40 MPa. During the cycle, the sample was loaded by axial vertical compression up to a maximum differential stress of 500 MPa. The AE activity and velocity changes were monitored by twelve P-wave and eight S-wave piezoelectric sensors. The ultrasonic measurements of the P-wave velocity revealed that the originally isotropic sample became anisotropic under axial loading. The P-wave velocity decreased in the horizontal direction and slightly increased in the vertical direction during loading (Fig. 8a). Concurrently, the P-wave attenuation increased in the horizontal direction and slightly decreased in the vertical direction (Fig. 8d). After unloading, the sample became again isotropic. The strength of the P-wave anisotropy developed during the loading cycle increased up to 24%.
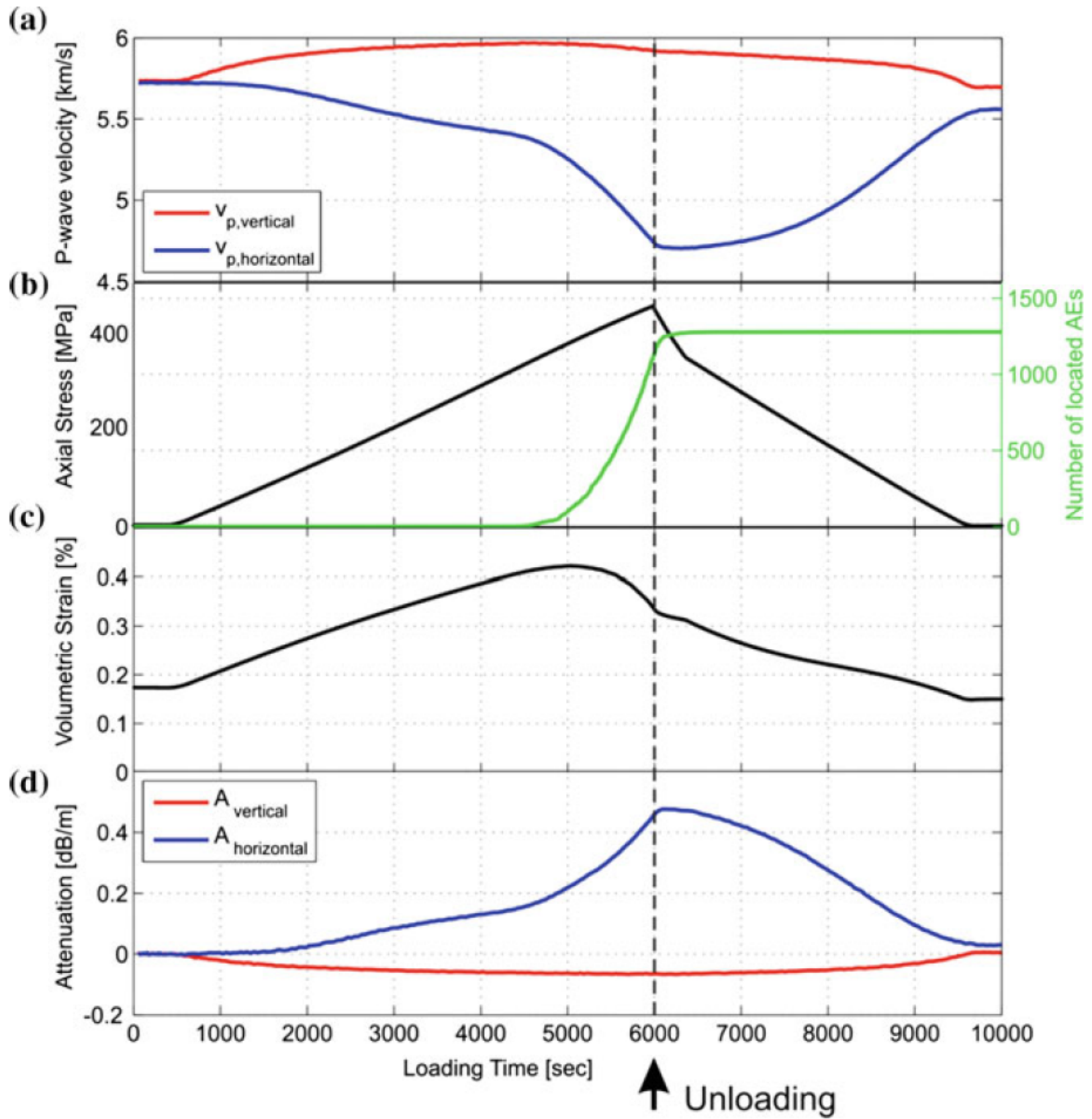
Fig. 8 **a** Vertical and horizontal *P*-wave velocities, **b** applied axial stress and acoustic emission rate, and **c** volumetric strain measured by Stanchits et al. (2006). Plot **d** shows the relative horizontal attenuation (blue line) and the relative vertical attenuation (red line) derived from ultrasonic transmission data after Stanchits et al. (2003, their Eq. 3). The horizontal confining pressure was 40 MPa during the loading cycle. After Stiele et al. (2016)

The moment and source tensors of observed AEs (Fig. 9) were calculated using three velocity models: anisotropic attenuating model, isotropic attenuating model and anisotropic elastic model. The parameters of velocity anisotropy of the sample were taken from ultrasonic measurements (Fig. 8a). The results revealed that neglecting the velocity anisotropy had a significant impact on the retrieved moment tensors. The P/T axes of the source tensors (Fig. 10b, upper plot) were highly scattered. By contrast, if anisotropy was considered and the source tensors correctly calculated (Fig. 10a, c, upper plots), the P/T axes were physically reasonable and in correspondence with the applied stress regime.
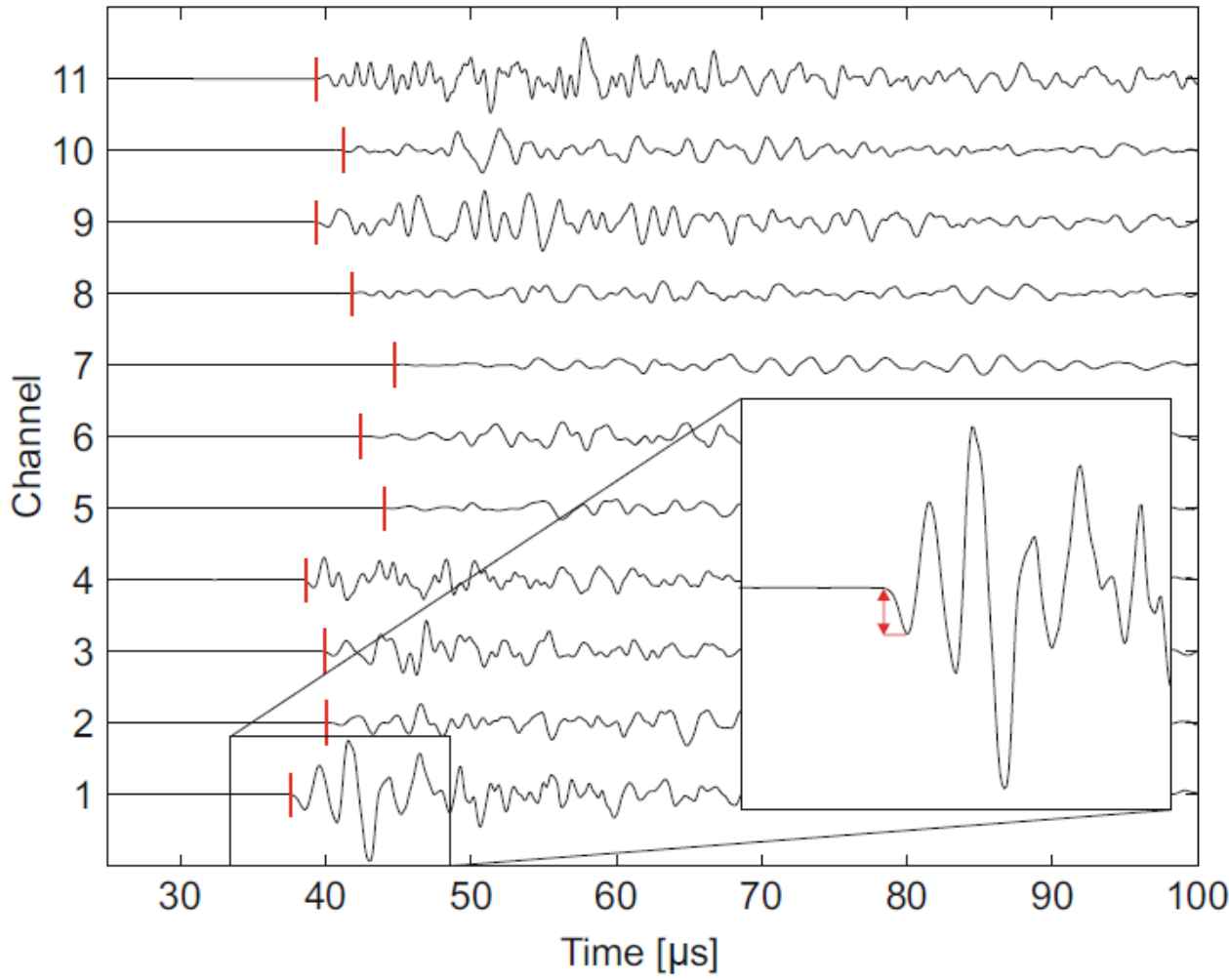
Fig. 9 Waveforms of an AE. Red vertical lines mark *P*-wave arrivals. The inset shows how *P*-wave amplitudes, used in the moment tensor inversion, were measured. After Stiele et al. (2016)

The non-DC components of the moment and source tensors were stable in all three inversions (Fig. 10, source-type plots). The ISO and CLVD components were predominantly positive indicating that mainly tensile (opening) cracks were activated. The scatter in the CLVD component was higher than that in the ISO component indicating that the errors in the velocity model mainly disturbed the CLVD component. Stierle et al. (2016) also proved that the moment tensor inversion applied to a large dataset of AEs can be utilized to determine anisotropic attenuation parameters of the rock sample.

4.2 Microearthquakes Induced During the 2000 Fluid-Injection Experiment at the KTB Site, Germany

The site of the KTB superdeep deep drilling borehole in Germany is characterized by a complex and heterogeneous crystalline crust (Emmerman and Lauterjung 1997) consisting of inclined alternating felsic and mafic layers, with mainly biotite gneiss and amphibolite (Rabbel et al. 2004). Field mapping, regional geophysics, and borehole results indicate that the region can be viewed as a block of steeply dipping foliated rocks with a uniform N330°E strike (Berkhemer et al. 1997; Okaya et al. 2004). In such rocks, preferred orientations of minerals prevail, and the crust may display a significant anisotropy which might be as high as 10–15% for *P* waves, and similar or even higher for *S* waves (Babuška and Cara 1991).
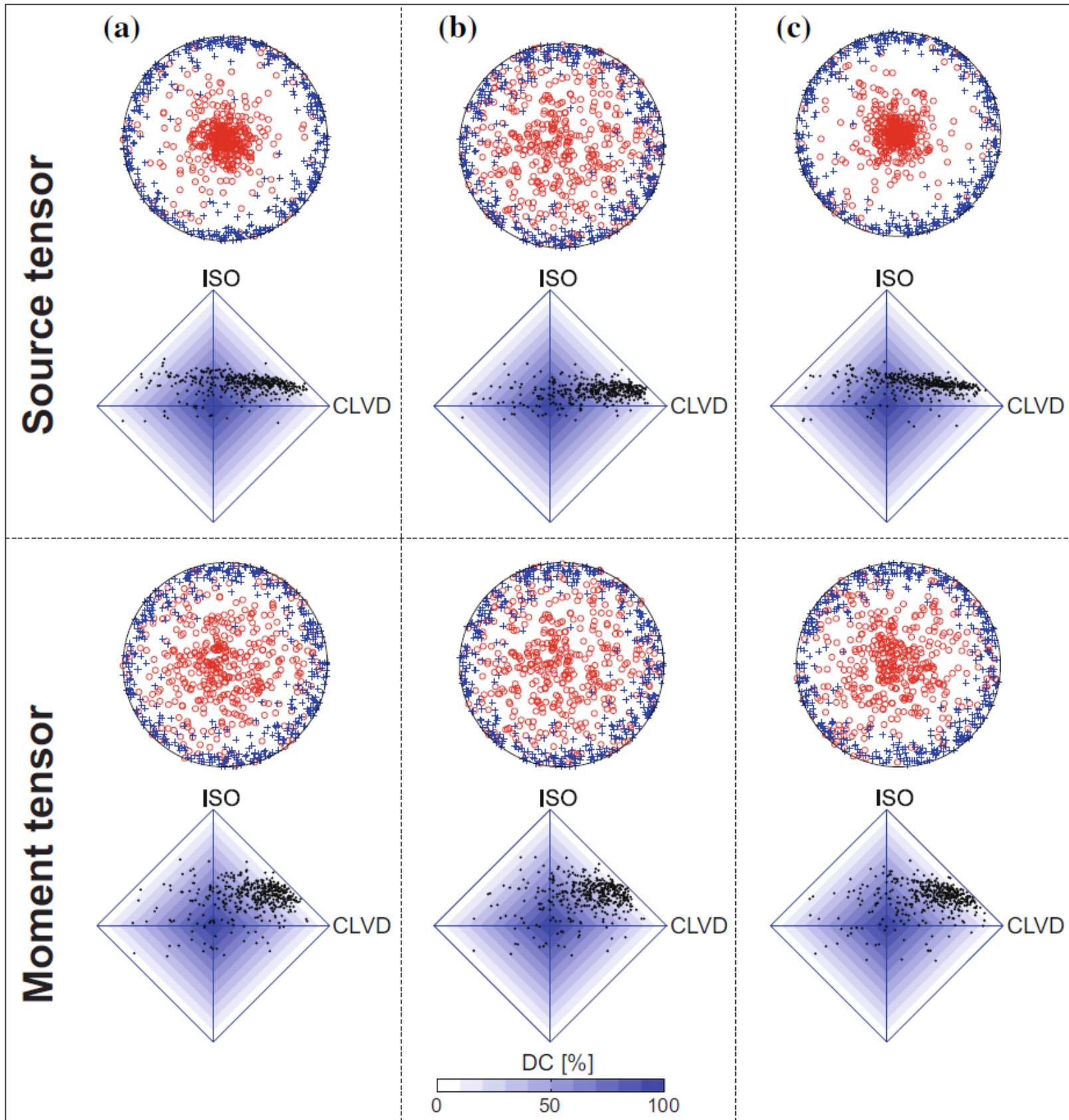
Fig. 10 Moment and source tensor inversions of observed AEs. The *P* axes (red circles in focal spheres) and *T* axes (blue plus signs in focal spheres) and the non-DC components (black dots in diamond plots) are calculated for the source tensors (upper plots) and moment tensors (lower plots) of AEs in: **a** anisotropic attenuating model, **b** isotropic attenuating model, and **c** anisotropic elastic model. The CLVD and ISO percentages are calculated by using Eq. (8) of Vavryčuk (2001a). After Stierle et al. (2016)

In 2000, a 60-day long-term fluid injection experiment was performed at the KTB site (Baisch et al. 2002). About 4000 m³ of water were injected into the well head to induce microseismicity. The entire borehole was pressurized and the well head pressure gradually increased during the experiment from 20 to 30 MPa. The seismicity was monitored by a surface network of 40 three-component seismic stations and by one downhole three-component sensor at a depth of 3.8 km, situated at the nearby pilot hole (Fig. 11). A total of 2799 induced microearthquakes were detected at the downhole sensor, and 237 of them were located using records at the surface
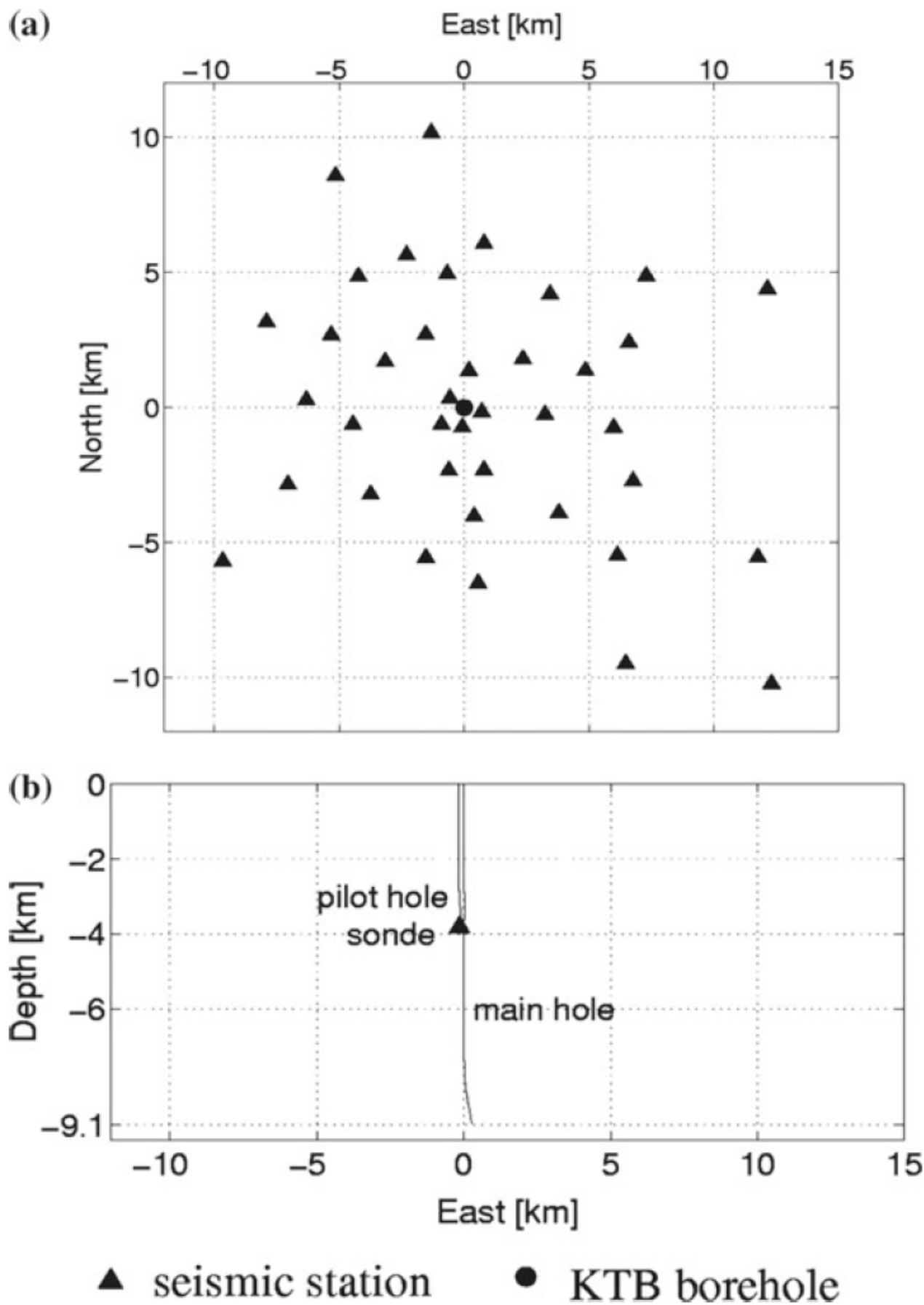
Fig. 11 The temporary seismic network operating during the 2000 injection experiment. **a** Map view of the network. The position of the KTB main hole is indicated by the dot. **b** Cross view of the main and pilot holes (view from the south). After Bohnhoff et al. (2004)

stations (Baisch et al. 2002). Fault plane solutions have been calculated for 125 events by Bohnhoff et al. (2004) and full moment tensors for 37 selected events by Vavryčuk et al. (2008). The retrieved moment tensors displayed significant non-DC components.

   Vavryčuk et al. (2008) adopted four alternative anisotropy models, published by Jahns et al. (1996) and Rabbel et al. (2004) obtained from VSP data, sonic logs and from laboratory measurements, and inverted the non-DC components of the moment tensors for the optimum orientation of anisotropy. The anisotropy orientation was sought over a sphere in a 5° grid of spherical angles. The misfit function was

Fig. 12 A comparison of
retrieved orientations of
anisotropy axes from
moment tensors for several
alternative models of
anisotropy with the
orientations of anisotropy
published by Rabbel et al.
(2004, a model for the depth
range of 0–8 km). After
Vavryčuk et al. (2008)
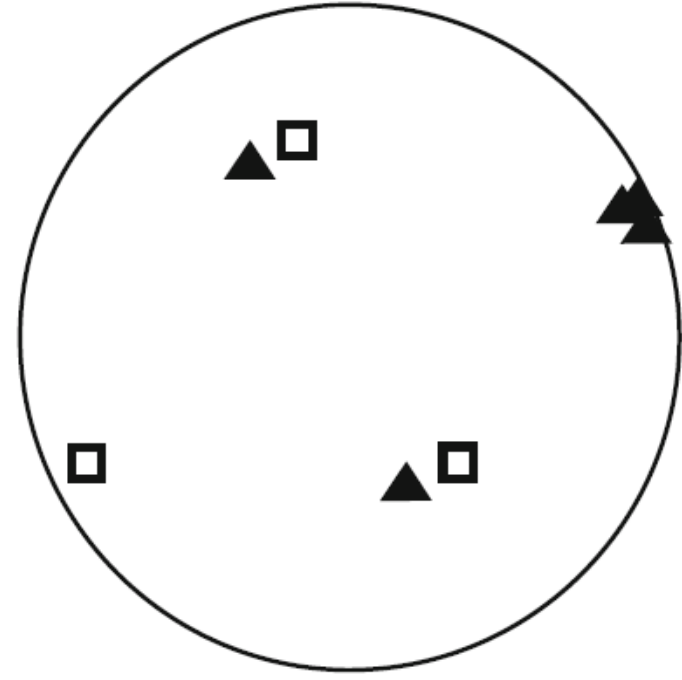
calculated by using Eq. (25) as the sum of determinants of source tensors of all
earthquakes under study. Hence, no a priori assumption about any specific type of
faulting was made, and the inversion was applicable not only to shear but also to
non-shear earthquakes.

The moment tensors retrieved by Vavryčuk et al. (2008) contained about 60% of
the DC component and 40% of the non-DC components. The ISO and CLVD compo-
nents were mutually uncorrelated. The errors of the non-DC components produced
by noise and by limitations of input data were suppressed by analysing only the most
reliable moment tensors determined for excellent ray coverage of the focal sphere.
The optimum orientation of the symmetry plane of transverse isotropy inferred from
the non-DC components was nearly vertical (see a nearly horizontal symmetry axis in
Fig. 12) with a strike typical for many major lithological units in the area (Rabbel et al.
2004; Okaya et al. 2004). After removing the anisotropy effects from the non-DC
components, the distribution of the ISO of the source tensors significantly narrowed
(Fig. 13). The ISO and CLVD of the source tensors became correlated with the corre-
lation coefficient of 0.6 for the most confident source tensors (Vavryčuk et al. 2008).
This indicated that the non-DC components originated jointly in seismic anisotropy
and in tensile faulting due to the fluid injection.

4.3   Deep-Focus Earthquakes in the Tonga Subduction Zone

Deep-focus earthquakes are particularly suitable for studying the sensitivity of
moment tensors to seismic anisotropy because: (1) they occur in subducting slabs,
which are assumed to be anisotropic (Fukao 1984; Kendall and Thomson 1993;
Hiramatsu et al. 1997; McNamara et al. 2002); (2) the surrounding mantle is nearly
isotropic, (3) the moment tensors of deep earthquakes are determined with a high
accuracy; and (4) they often display non-DC components (Dziewonski et al. 2001,
2003; Sipkin 1986). It is speculated that anisotropy in the slab is caused by an align-
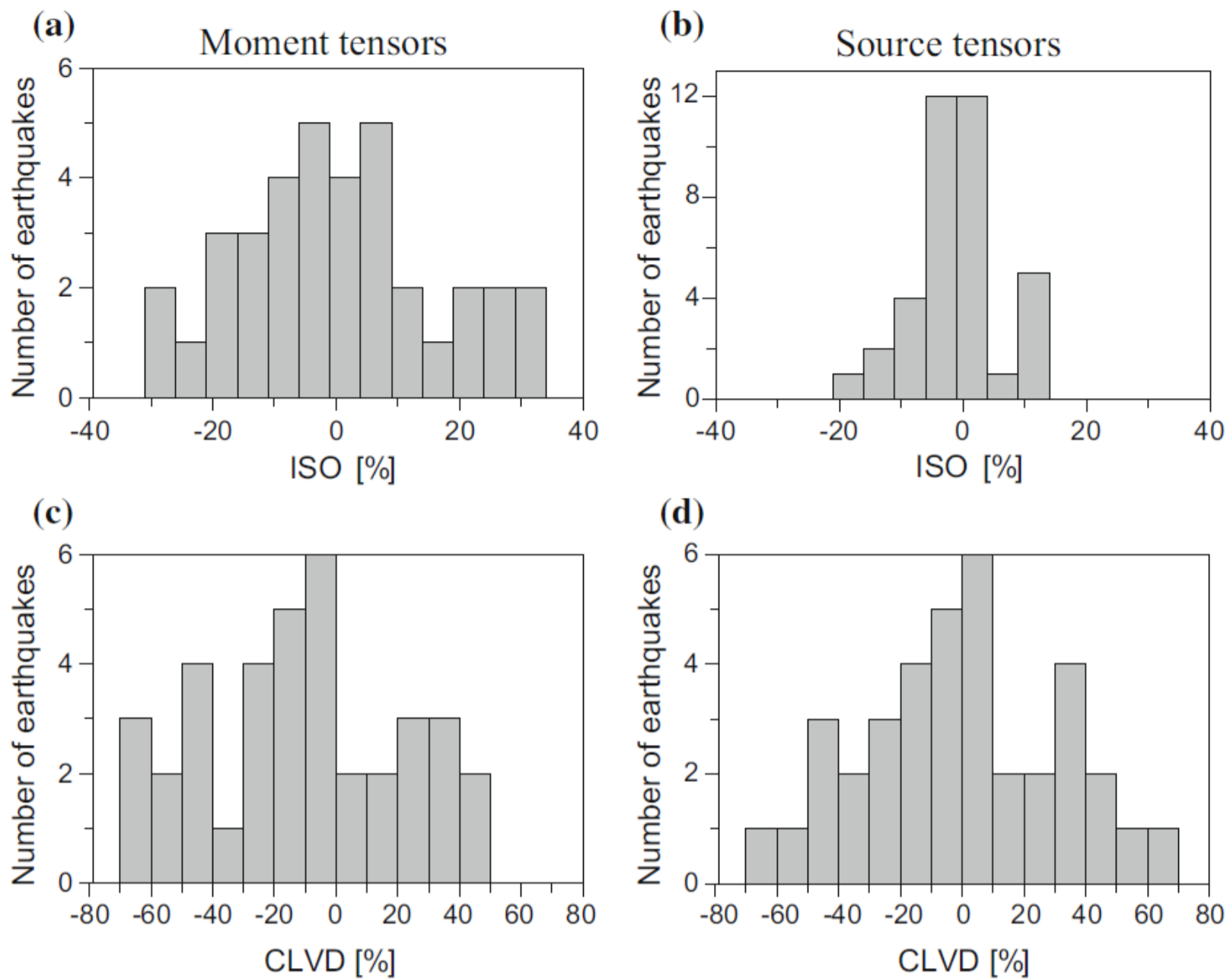ment of metastable olivine and its polymorphs wadsleyte and ringwoodite, or the

Fig. 13 Histograms of the percentages of the ISO (**a, b**) and CLVD (**c, d**) components of the moment tenors (left-hand plots) and source tensors (right-hand plots). The CLVD and ISO percentages are calculated by using Eq. (8) of Vavryčuk (2001a). For details, see Vavryčuk et al. (2008)

ilmenite form of pyroxene (Anderson 1987; Mainprice et al. 2000). The intra-slab anisotropy can also be induced by strain due to large stresses generated when a rigid slab encounters the 670 km discontinuity (Wookey et al. 2002).

Vavryčuk (2004, 2006) analysed the moment tensors of deep earthquakes in the Tonga-Kermadec subduction zone, which is the most active zone in the world and offers a largest dataset of moment tensors of deep earthquakes. The deep part of the Tonga subduction zone consists of two differently oriented slab segments (Fig. 14a): the northern segment within latitudes 17–19° S, and the southern segment within latitudes 19.5–27° S. Both segments are seismically active at depths from 500 to 700 km. The mechanisms of deep-focus earthquakes reported in the Harvard moment tensor catalogue (Dziewonski et al. 2001, 2003) contain CLVD components that behave differently in both segments. The mean absolute value of the CLVD is 12% for the northern segment and 16% for the southern segment (Fig. 14b). The complex behaviour of the CLVD is explained by spatially dependent seismic anisotropy in the slab.

The inversion for anisotropy from the non-DC components of moment tensors performed by Vavryčuk (2004, 2006) pointed to orthorhombic anisotropy in the both
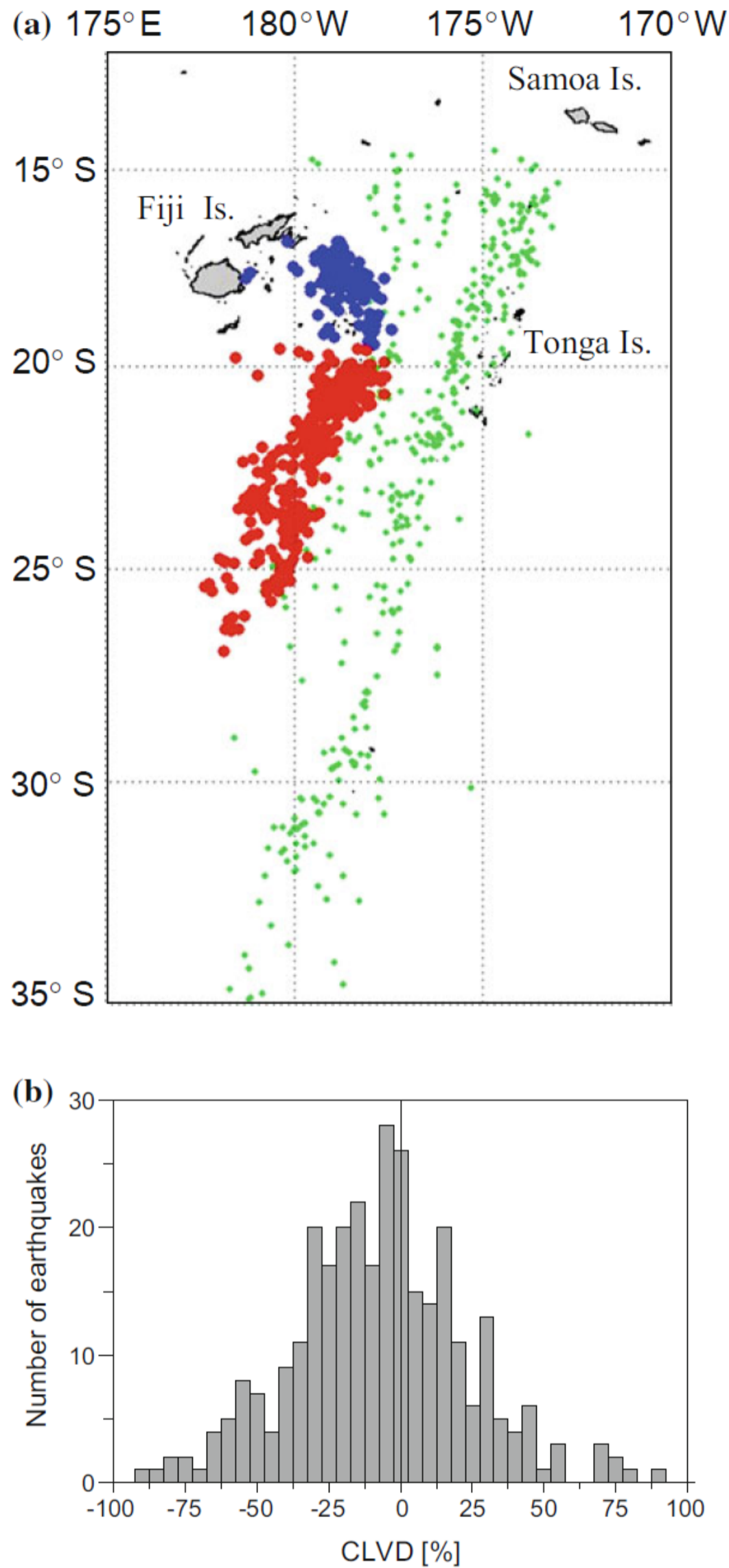
Fig. 14 **a** Epicentres of earthquakes in the Tonga subduction zone. Blue and red dots mark the deep-focus earthquakes with depth > 500 km in the northern and southern segment, respectively. Green dots mark the other earthquakes in the region (depth > 100 km). **b** Histogram of the CLVD of moment tensors for the deep earthquakes in the southern cluster. The CLVD percentages are calculated by using Eqs. (8a–c) of Vavryčuk (2001a). After Vavryčuk (2004)
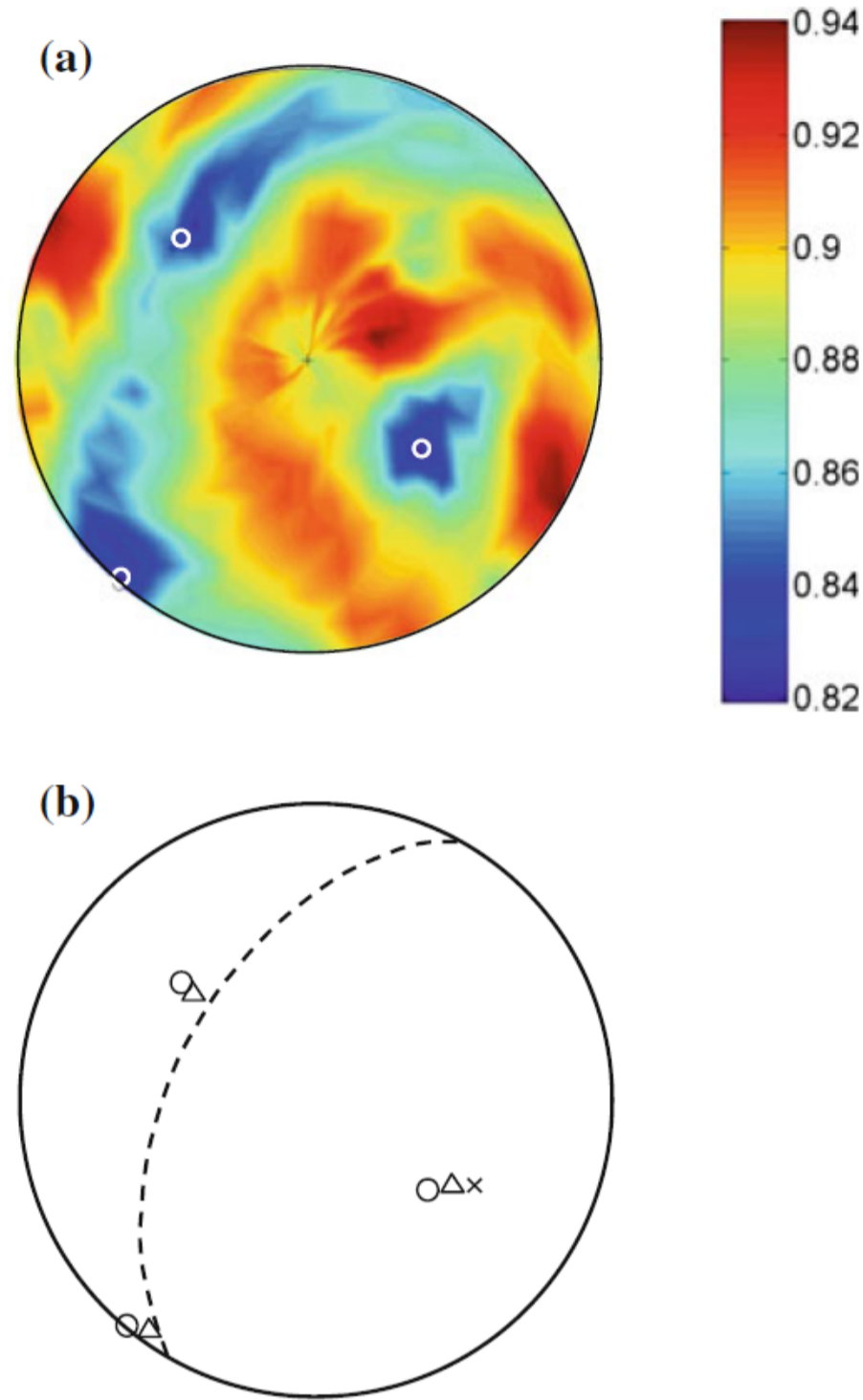
(a)

(b)

Fig. 15 Inversion for orthorhombic anisotropy using moment tensors of deep-focus earthquakes in the southern segment. **a** Misfit function for the symmetry axes of orthorhombic anisotropy normalized to the misfit for an isotropic medium and displayed in the lower hemisphere equal-area projection. The optimum directions of the symmetry axes of anisotropy are marked by circles. **b** A comparison of slab, stress and anisotropy orientations. The directions of the slab normal (x), of the principal stress axes (triangles) calculated from focal mechanisms, and of the symmetry axes of anisotropy (circles) calculated from moment tensors. The lower-hemisphere equal-area projection is used. The dashed line shows the intersection of the slab with the hemisphere Modified after Vavryčuk (2004)

slab segments. The anisotropy was of a uniform strength of 5–7% for the P waves and of 9–12% for the S waves, and was oriented according to the orientation of each segment and the stress acting in it (Fig. 15 for the southern segment). The spatial variation of velocities was roughly similar in both segments (Fig. 16 for the southern segment). The retrieved anisotropy might have several possible origins. It can be: (1) intrinsic, caused by preferentially aligned anisotropic minerals such as wadsleyite, ringwoodite, ilmenite or others, (2) effective, caused, for example, by intra-slab layering, or (3) partly apparent, produced by systematic errors in the moment tensors due to neglecting 3D slab geometry and the slab/mantle velocity contrast when calculating the Green functions in the moment tensor inversion.

Fig. 16 Spatial variation of
the velocity in the southern
slab segment predicted by
the optimum anisotropy
model for the *P* (**a**), *S*1 (**b**)
and *S*2 (**c**) waves. Lower
hemisphere equal-area
projection is used. Directions
of the symmetry axes are
marked by circles. After
Vavryčuk (2004)
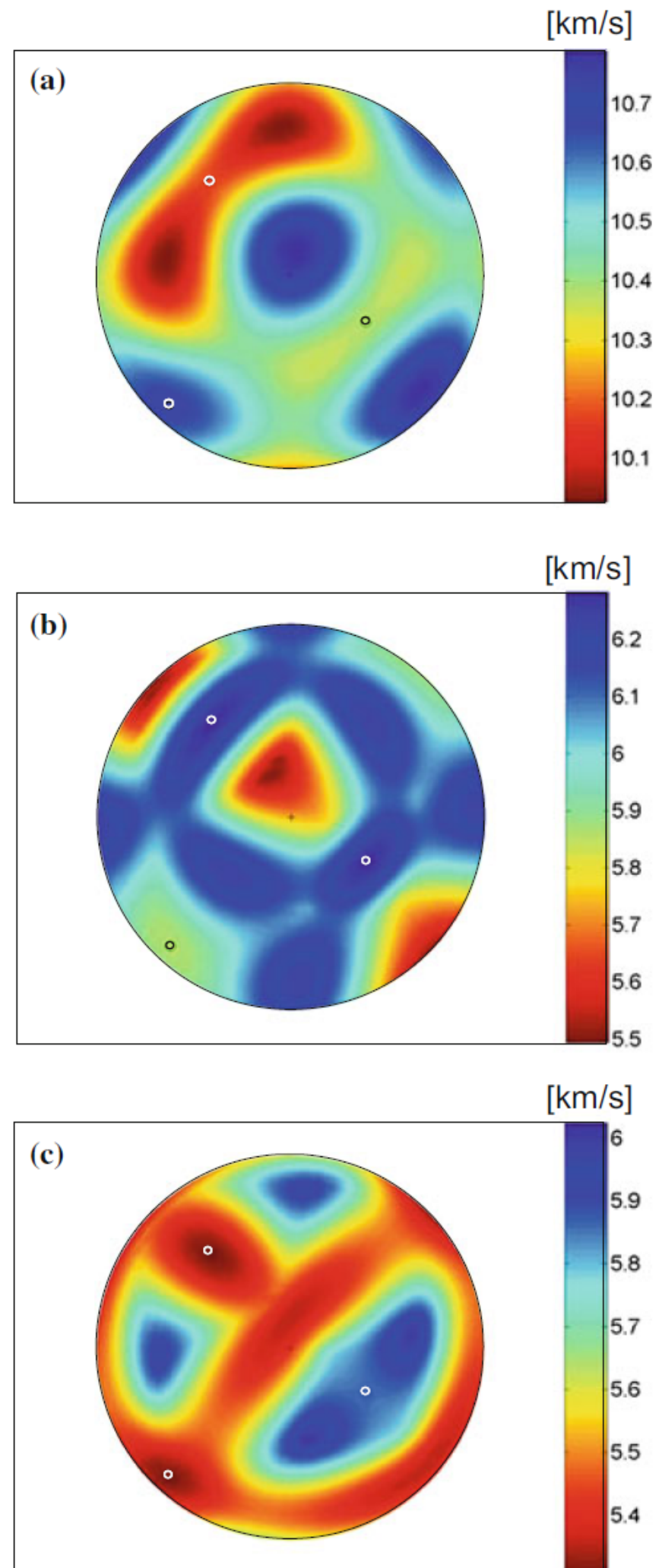
5 Discussion and Conclusions

Moment tensors are quite sensitive to seismic anisotropy of rocks. Neglect of
anisotropy in the moment tensor inversion reduces the accuracy of the retrieved
DC and non-DC components of the moment and source tensors. The errors in the
non-DC components are mainly projected into the CLVD component, which usually
displays about three times higher scatter than the ISO component.

Shear faulting on planar faults in anisotropic media can produce non-DC mechanisms. The amount of the CLVD and ISO depends on strength and symmetry of anisotropy and on the orientation of faulting. The fault plane solutions in anisotropy are characterized by the same ambiguity in identifying a fault normal and slip direction as in isotropy. The moment tensor corresponding to shear faulting in anisotropy has eigenvectors (P, T and B axes) that can deviate from those in isotropy. If anisotropy is neglected at a focal area, the fault plane and slip calculated under the isotropic assumption can deviate from true ones.

Shear faulting in anisotropic rocks present in the Earth's crust, Earth's mantle or in the subduction zones can produce mechanisms with significant non-DC components. The CLVD can typically attain values up to 30%, and the ISO up to 15%. The fault plane solutions calculated under the assumption of isotropy typically deviate from the true solutions by the angle of 5°–10°. However, for strongly anisotropic rocks such as some shales or shists, the CLVD and ISO can be much higher, and the isotropic procedure for determining the fault plane solution can completely fail (Vavryčuk 2005).

If the focal zone is anisotropic, the moment tensors can be utilized for determining parameters of anisotropy. The inversion of moment tensors for anisotropy is advantageous because it yields a local value of anisotropy just in the focal area. Hence it should, in principle, be capable of retrieving the anisotropy of a focal area that is surrounded by a differently anisotropic or by isotropic medium. The case when the surrounding medium is differently anisotropic is particularly complicated for standard methods, because the effects of focal anisotropy can easily be masked by those of the surrounding medium. In addition, the inversion of moment tensors for anisotropy is very robust. If a large set of high-quality moment tensors is available, the inversion can retrieve the orientation and strength of anisotropy even for low anisotropy symmetries as for orthorhombic symmetry. For example, the method was capable to retrieve the orientation and strength of the P, $S1$ and $S2$ anisotropy in the Tonga subduction zone (Vavryčuk 2004, 2006).

References

Anderson DL (1987) Thermally induced phase changes, lateral heterogeneity of the mantle, continental roots and deep slab anomalies. J Geophys Res 92:13968–13980

Aki K, Richards PG (2002) Quantitative seismology. University Science Books, Sausalito

Babuška V, Cara M (1991) Seismic anisotropy in the Earth. Kluwer Academic Publisher, London

Baisch S, Bohnhoff M, Ceranna L, Tu Y, Harjes H-P (2002) Probing the crust to 9 km depth: fluid injection experiments and induced seismicity at the KTB superdeep drilling hole, Germany. Bull Seism Soc Am 92:2369–2380

Ben-Menahem A, Sena AG (1990a) Seismic source theory in stratified anisotropic media. J Geophys Res 95:15395–15427

Ben-Menahem A, Sena AG (1990b) The elastodynamic Green's tensor in an anisotropic half-space. Geophys J Int 102:421–443

Berckhemer H, Rauen A, Winter H, Kern H, Kontny A, Lienert M, Nover G, Pohl J, Popp T, Schult A, Zinke J, Soffel HC (1997) Petrophysical properties of the 9-km-deep crustal section at KTB. J Geophys Res 102:18337–18361

Bohnhoff M, Baisch S, Harjes H-P (2004) Fault mechanisms of induced seismicity at the superdeep German Continental Deep Drilling Program (KTB) borehole and their relation to fault structure and stress field. J Geophys Res 109:B02309. https://doi.org/10.1029/2003jb002528

Burridge R (1967) The singularity on the plane lids of the wave surface of elastic media with cubic symmetry. Q J Mech Appl Math 20:40–56

Crampin S (1993) A review of the effects of crack geometry on wave propagation through aligned cracks. Can J Expl Geophysics 29:3–17

Červený V (2001) Seismic ray theory. Cambridge University Press, Cambridge

Dziewonski AM, Ekström G, Maternovskaya NN (2001) Centroid moment tensor solutions for July–September 2000. Phys Earth Planet Inter 124:9–23

Dziewonski AM, Ekström G, Maternovskaya NN (2003) Centroid moment tensor solutions for October–December 2000. Phys Earth Planet Inter 136:145–164

Emmerman R, Lauterjung J (1997) The German Continental Deep Drilling Program KTB: overview and major results. J Geophys Res 102:18179–18201

Frohlich C (1994) Earthquakes with non-double-couple mechanisms. Science 264:804–809

Fukao Y (1984) Evidence from core-reflected shear waves for anisotropy in the Earth's mantle. Nature 309:695–698

Gajewski D (1993) Radiation from point sources in general anisotropic media. Geophys J Int 113:299–317

Helbig K (1994) Foundations of anisotropy for exploration seismics. Pergamon, New York

Hiramatsu Y, Ando M, Ishikawa Y (1997) ScS wave splitting of deep earthquakes around Japan. Geophys J Int 128:409–424

Hudson JA (1981) Wave speeds and attenuation of elastic waves in material containing cracks. Geophys J R astr Soc 64:133–150

Jahns E, Rabbel W, Siegesmund S (1996) Quantified seismic anisotropy at different scales: a case study from the KTB crustal segment. J Geol Wiss 24:729–740

Julian BR, Miller AD, Foulger GR (1998) Non-double-couple earthquakes, 1 Theory. Rev Geophys 36:525–549

Kaneshima S, Ando M, Kimura S (1988) Evidence from shear-wave splitting for the restriction of seismic anisotropy to the upper crust. Nature 335:627–629

Kawakatsu H (1991) Enigma of earthquakes at ridge-transform-fault plate boundaries—distribution of non-double-couple parameter of Harvard CMT solutions. Geophys Res Lett 18:1103–1106

Kawasaki I, Tanimoto T (1981) Radiation patterns of body waves due to the seismic dislocation occurring in an anisotropic source medium. Bull Seismol Soc Am 71:37–50

Kendall J-M, Thomson C (1993) Seismic modelling of subduction zones with inhomogeneity and anisotropy—I Teleseismic P-wavefront tracking. Geophys J Int 112:39–66

Kern H, Schmidt R (1990) Physical properties of KTB core samples at simulated in situ conditions. Sci Drill 1:217–223

Mainprice D, Barruol G, Ben Ismail W (2000) The seismic anisotropy of the Earth's mantle: from single crystal to polycrystal. In: Forte A, Liebermann RC, Masters G, Stixrude L, Karato S (eds) Earth's deep interior, mineral physics and tomography from the atomic to the global scale. Geophysical monograph series. American Geophysical Union, Washington, pp 237–264

McNamara AK, van Keken PE, Karato S (2002) Development of anisotropic structure in the Earth's lower mantle by solid-state convection. Nature 416:310–314

Miller AD, Foulger GR, Julian BR (1998) Non-double-couple earthquakes, 2 observations. Rev Geophys 36:551–568

Musgrave MJP (1970) Crystal acoustics. Holden Day, San Francisco

Okaya D, Rabbel W, Beilecke T, Hasenclever J (2004) P wave material anisotropy of tectono-metaorphic terrane: an active source seismic experiment at the KTB super-deep drill hole, southeast Germany. Geophys Res Lett 31:L24620. https://doi.org/10.1029/2004gl020855

Pros Z, Lokajíček T, Klíma K (1998) Laboratory approach to the study of elastic anisotropy on rock samples. Pure Appl Geophys 151:619–629

Pšenčík I (1998) Green functions for inhomogeneous weakly anisotropic media. Geophys J Int 135:279–288

Rabbel W, Beilecke T, Bohlen T, Fischer D, Frank A, Hasenclever J, Born G, Kück J, Bram K, Druivenga G, Lüschen E, Gebrande H, Pujol J, Smithson S (2004) Superdeep vertical seismic profiling at the KTB deep drill hole (Germany): seismic close-up view of a major thrust zone down to 85 km depth. J Geophys Res 109:B09309. https://doi.org/10.1029/2004jb002975

Rabbel W, Mooney WD (1996) Seismic anisotropy of the crystalline crust: what does it tell us? Terra Nova 8:16–21

Rössler D, Rümpker G, Krüger F (2003) Ambiguous moment tensors and radiation patterns in anisotropic media with applications to the modeling of earthquake mechanisms in W-Bohemia. Stud Geophys Geod 48:233–250

Savage MK (1999) Seismic anisotropy and mantle deformation: what have we learned from shear wave splitting? Rev Geophys 37:65–106

Shearer PM, Chapman CH (1989) Ray tracing in azimuthally anisotropic media—I. Results for models of aligned cracks in the upper crust. Geophys J Int 96:51–64

Šílený J, Vavryčuk V (2000) Approximate retrieval of the point source in anisotropic media: numerical modelling by indirect parametrization of the source. Geophys J Int 143:700–708. https://doi.org/10.1046/j1365-246x200000256x

Šílený J, Vavryčuk V (2002) Can unbiased source be retrieved from anisotropic waveforms by using an isotropic model of the medium? Tectonophysics 356:125–138. https://doi.org/10.1016/s0040-1951(02)00380-3

Silver PG (1996) Seismic anisotropy beneath the continents: probing the depths of geology. Ann Rev Earth Planet Sci 24:385–432

Sipkin SA (1986) Interpretation of non-double-couple earthquake mechanisms derived from moment tensor inversion. J Geophys Res 91:531–547

Stanchits SA, Lockner DA, Ponomarev AV (2003) Anisotropic changes in P-wave velocity and attenuation during deformation and fluid infiltration of granite. Bull Seism Soc Am 93(4):1803–1822

Stanchits S, Vinciguerra S, Dresen G (2006) Ultrasonic velocities, acoustic emission characteristics and crack damage of basalt and granite. Pure App Geophys 163(5–6):975–994

Stierle E, Vavryčuk V, Kwiatek G, Charalampidou E-M, Bohnhoff M (2016) Seismic moment tensors of acoustic emissions recorded during laboratory rock deformation experiments: sensitivity to attenuation and anisotropy. Geophys J Int 205(1):38–50. https://doi.org/10.1093/gji/ggw009

Svitek T, Vavryčuk V, Lokajíček T, Petružálek M (2014) Determination of elastic anisotropy of rocks from P- and S-wave velocities: numerical modelling and lab measurements. Geophys J Int 199(3):1682–1697. https://doi.org/10.1093/gji/ggu332

Vavryčuk V (1997) Elastodynamic and elastostatic Green tensors for homogeneous weak transversely isotropic media. Geophys J Int 130:786–800. https://doi.org/10.1111/j.1365-246x.1997.tb01873.x

Vavryčuk V (2001a) Inversion for parameters of tensile earthquakes. J Geophys Res 106:16339–16355. https://doi.org/10.1029/2001jb000372

Vavryčuk V (2001b) Ray tracing in anisotropic media with singularities. Geophys J Int 145:265–276. https://doi.org/10.1046/j0956-540x200101387x

Vavryčuk V (2002) Non-double-couple earthquakes of 1997 January in West Bohemia, Czech Republic: evidence of tensile faulting. Geophys J Int 149:364–373. https://doi.org/10.1046/j.1365-246x.2002.01654.x

Vavryčuk V (2003) Parabolic lines and caustics in homogeneous weakly anisotropic solids. Geophys J Int 152:318–334. https://doi.org/10.1046/j1365-246x200301845x

Vavryčuk V (2004) Inversion for anisotropy from non-double-couple components of moment tensors. J Geophys Res 109:B07306. https://doi.org/10.1029/2003jb002926

Vavryčuk V (2005) Focal mechanisms in anisotropic media. Geophys J Int 161:334–346. https://doi.org/10.1111/j1365-246x200502585x

Vavryčuk V (2006) Spatially dependent seismic anisotropy in the Tonga subduction zone: a possible contributor to the complexity of deep earthquakes. Phys Earth Planet Inter 155:63–72. https://doi.org/10.1016/jpepi200510005

Vavryčuk V (2007) Asymptotic Green's function in homogeneous anisotropic viscoelastic media. Proc R Soc A 463:2689–2707. https://doi.org/10.1098/rspa20071862

Vavryčuk V (2011) Tensile earthquakes: theory, modeling, and inversion. J Geophys Res 116(B12):B12320. https://doi.org/10.1029/2011jb008770

Vavryčuk V (2015) Moment tensor decompositions revisited. J Seismol 19(1):231–252. https://doi.org/10.1007/s10950-014-9463-y

Vavryčuk V, Bohnhoff M, Jechumtálová Z, Kolář P, Šílený J (2008) Non-double-couple mechanisms of micro-earthquakes induced during the 2000 injection experiment at the KTB site, Germany: a result of tensile faulting or anisotropy of a rock? Tectonophysics 456:74–93. https://doi.org/10.1016/jtecto200708019

Vernik L, Liu X (1997) Velocity anisotropy in shales: a petrological study. Geophysics 62:521–532

Wookey J, Kendall J-M, Barruol G (2002) Mid-mantle deformation inferred from seismic anisotropy. Nature 415:777–780